LETTERS
https://doi.org/10.1038/s41566-021-00862-3

nature photonics

Anomalous upconversion amplification induced by surface reconstruction in lanthanide sublattices

Hui Xu[1,6] ✉, Sanyang Han[2,6], Renren Deng[2], Qianqian Su[2], Ying Wei[3], Yongan Tang[2], Xian Qin[2] ✉ and Xiaogang Liu[2,4,5] ✉

Upconversion nanocrystals have been extensively investigated for optical imaging and biomedical applications[1,2]. However, their photoluminescence is strongly attenuated by surface quenching as the nanocrystal size diminishes[3]. Despite considerable efforts[4,5], the quenching mechanism remains poorly understood. Here we report that surface coordination of bidentate picolinic acid molecules to $NaGdF_4$:Yb/Tm nanoparticles enhances four-photon upconversion by 11,000-fold. Mechanistic studies indicate that surface ligand coordination reconstructs orbital hybridization and crystal-field splitting, minimizing the energy difference between the 4*f* orbitals of surface and inner lanthanide sensitizers. The 4*f*-orbital energy resonance facilitates energy migration within the ytterbium sublattice, impeding energy diffusion to surface defects and ultimately enhancing energy transfer to the emitters. Moreover, ligand coordination can exert energy-level reconstruction with a ligand–sensitizer separation of over 2 nm. These findings offer insights into the development of highly emissive nanohybrids and provide a platform for constructing optical interrogation systems at single-particle levels.

Lanthanide-doped inorganic nanocrystals possess abundant 4*f* electronic states, enabling multiphoton upconversion without the stringent conditions imposed by two-photon absorption and multiple harmonic generation, which require phase matching or coherent pumping[1,6]. Energy-transfer upconversion is the most efficient upconversion process under low-power irradiation[7–9]. Owing to their high photostability and colour tunability[10,11], lanthanide-doped upconversion nanocrystals have been used for various applications, ranging from anticounterfeiting to lasing and super-resolution imaging[12–15]. By exploiting excitation in biological windows, researchers have extended the application of upconversion nanocrystals to blood-vessel imaging, optogenetics, immunotherapy and drug delivery[16–19]. In these applications, ultrasmall nanocrystals with high brightness become crucial[20,21]. However, the use of protein-sized nanocrystals is generally constrained by severe surface quenching, substantially reducing their luminescence brightness and conversion efficiency[4,22,23].

Passivation of upconversion nanocrystals with an optically inactive shell suppresses surface quenching but inevitably enlarges the particle size. Other approaches, which involve high-power excitation to saturate the excited states of lanthanide ions and compensate for surface-mediated energy loss, have proven effective in enhancing the emission intensity[3,24–27]. Although successful, high-power irradiation causes tissue damage and requires complex instrumentation. Attaining high brightness in ultrasmall upconversion nanoparticles remains a critical challenge because of complex optical pathways, including energy migration, cross-relaxation and deleterious vibronic dissipation. This complexity, along with the abundant energy levels of lanthanides, has hidden the underlying quenching mechanisms.

To understand surface-mediated excitation dynamics and how surface coordination influences the diffusion of excitation energy in upconversion nanocrystals, we mapped the coordination and electronic structures of Yb^{3+} ions occupying the interior and exterior of a hexagonal-phase $NaYF_4$ nanocrystal. The mapping was performed using quantum mechanical simulations based on density functional theory (DFT). In the crystal-structure analysis, an inner Yb^{3+} ion was ninefold coordinated by fluoride ions, while an Yb^{3+} ion exposed on the (0001) surface was coordinated with only six fluoride ions (Fig. 1a). Bader analysis showed that this surface Yb^{3+} ion remains trivalent. By contrast, incomplete surface coordination leads to reduced hybridization between the 4*f* orbitals of the Yb^{3+} ions and the 2*p* orbitals of the neighbouring F^- ions, shifting the occupied and empty 4*f* orbitals ($4f_{occ}$ and $4f_{emp}$, respectively) of the surface Yb^{3+} ions to lower and higher energy regions, respectively. Consequently, the $4f_{emp}$–$4f_{occ}$ energy gap (ΔE) of the surface Yb^{3+} ions was 0.28 eV higher than that of the inner Yb^{3+} ions. Given the coexistence of core-like and band-like 4*f* electrons[28], this energy change in 4*f* orbitals is mainly attributed to non-saturated coordination-reduced hybridization between band-like ytterbium 4*f* and fluorine 2*p* orbitals, along with weakened crystal-field splitting. The resulting orbital-energy mismatch ΔE suggests the existence of a mismatch between the 4*f* transition energies of the surface and inner Yb^{3+} ions, thereby reducing the efficiency of resonance-energy migration between these Yb^{3+} ions. Given the high surface-to-volume ratio of ultrasmall nanoparticles, a large portion of Yb^{3+} dopants is either directly exposed on the nanoparticle surfaces or proximal to the surfaces[29]. These outer-layer Yb^{3+} dopants are highly susceptible to surface-related non-radiative deactivation, limiting energy transfer to lanthanide emitters[5].

[1]Key Laboratory of Functional Inorganic Material Chemistry (Ministry of Education) and School of Chemistry and Material Science, Heilongjiang University, Harbin, China. [2]Department of Chemistry, National University of Singapore, Singapore, Singapore. [3]School of Electromechanical Engineering, Heilongjiang University, Harbin, China. [4]Joint School of National University of Singapore and Tianjin University, International Campus of Tianjin University, Fuzhou, China. [5]Center for Functional Materials, National University of Singapore Suzhou Research Institute, Suzhou, China. [6]These authors contributed equally: Hui Xu, Sanyang Han. ✉e-mail: hxu@hlju.edu.cn; chmqinx@nus.edu.sg; chmlx@nus.edu.sg

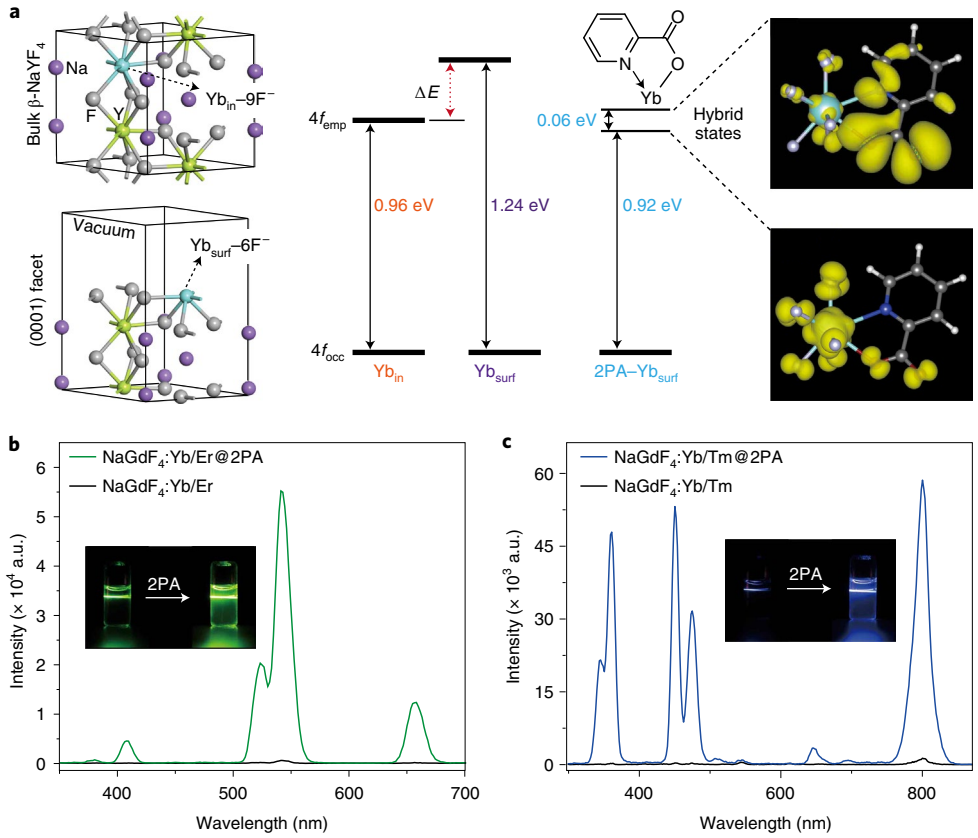

Fig. 1 | Multiphoton upconversion enhancement through surface reconstruction. a, Left: optimized atomic structures showing the first coordination sphere of ytterbium atoms residing in the interior (Yb_{in}, top) and exterior (Yb_{surf}, bottom) of a $NaLnF_4$ (Ln = Y or Gd) nanoparticle. Middle: simulated single-particle 4*f* energy levels of ytterbium atoms with nine-, six- and eightfold coordination configurations, respectively. $4f_{emp}$ and $4f_{occ}$ represent the lowest empty and highest occupied 4*f* orbitals of the ytterbium atom, respectively; ΔE is the energy difference between the $4f_{emp}$–$4f_{occ}$ gaps of the surface and inner ytterbium atoms. Right: spatial distribution of the partial charge densities of coupling states. Cyan, purple, grey, white, red and blue balls denote Yb, F, C, H, O and N atoms, respectively. **b**,**c**, Upconversion emission spectra of $NaGdF_4$:Yb/Er (18/2%) (**b**) and $NaGdF_4$:Yb/Tm (49/1%) (**c**) nanoparticles (10 nm) under 980 nm excitation, recorded in ethanol before and after coating with 2PA molecules. Insets are the corresponding photoluminescence images showing the emission changes in the ligand-free and 2PA-capped nanoparticles.

We reasoned that a rigid, strongly coordinated ligand could reconstruct the orbital hybridization and crystal-field splitting in the 4*f* orbitals of the surface Yb^{3+} ions, thereby minimizing the energy mismatch between the 4*f* orbitals of the surface and inner Yb^{3+} ions. The energy-level reconstruction can facilitate energy migration and activate dark surface layers of nanocrystals, thereby enhancing energy transfer to the emitters (for example, Er^{3+} or Tm^{3+}). To validate this hypothesis, we coordinated surface Yb^{3+} ions with molecules of pyridine-2-carboxylic acid (2PA), chosen for its highly rigid aromatic framework and bidentate coordination motif. The N,O-hybrid coordination site of the 2PA ligand enables the formation of a five-membered chelate ring with a surface Yb^{3+} ion. Our DFT calculations showed that when the nanoparticles are coated with 2PA ligands, orbital hybridization raises the occupied 4*f* levels of the surface Yb^{3+} ions and lowers their empty 4*f* levels. Consequently, the $4f_{emp}$–$4f_{occ}$ energy gap becomes comparable to that of the inner Yb^{3+} ions (Fig. 1a, Supplementary Figs. 1–8 and Supplementary Tables 1 and 2). As an added benefit, these rigid ligands can stabilize the excited state of the surface Yb^{3+} ions, protect the surface lanthanides from interacting with solvent molecules and suppress surface fluoride vacancy-induced quenching, largely minimizing multiphonon non-radiative decay.

We next prepared ligand-free $NaGdF_4$:Yb/X (X = Er or Tm) nanocrystals of ~10 nm in diameter (Supplementary Figs. 9 and 10). After coating with 2PA molecules, the upconversion luminescence of Yb/Er- and Yb/Tm-codoped nanoparticles was enhanced by 88- and 150-fold, respectively (Fig. 1b,c). Absorption spectroscopy of the as-prepared nanoparticles showed a negligible change in the near-infrared spectral region before and after 2PA attachment, suggesting that these ligands simultaneously enhanced the emission intensity and quantum efficiency (Supplementary Fig. 11 and Supplementary Table 3). The lifetime of Er^{3+} emitters in the $NaGdF_4$:Yb/Er nanocrystals increased after 2PA attachment with a delayed rise (Supplementary Fig. 11). This result is consistent with the increased emission lifetime (from 93 to 289 μs) of $NaGdF_4$:Yb nanocrystals under 965 nm excitation (Fig. 2a). The increased lifetime of 980 nm emission of the $Yb(2PA)_3$ complex further confirms surface Yb^{3+}–2PA coupling (Supplementary Fig. 12), suggesting that the 2PA coating activates the dark surface layer and promotes energy migration within the Yb^{3+} sublattices[30–32]. This energy migration facilitates excitation energy diffusion within the sensitizer sublattice and energy transfer to the emitters. Unlike molecularly engineered nanohybrids involving energy transfer between lanthanides and molecular triplet states[33,34], 2PA ligands may behave as pseudoatoms that participate in orbital hybridization and support the crystal field for surface lanthanides. Notably, 2PA-coordinated nanocrystals are resistant to a series of organic solvents, and they remain highly emissive even after 120 minutes of continuous laser irradiation (Supplementary Figs. 13–15).

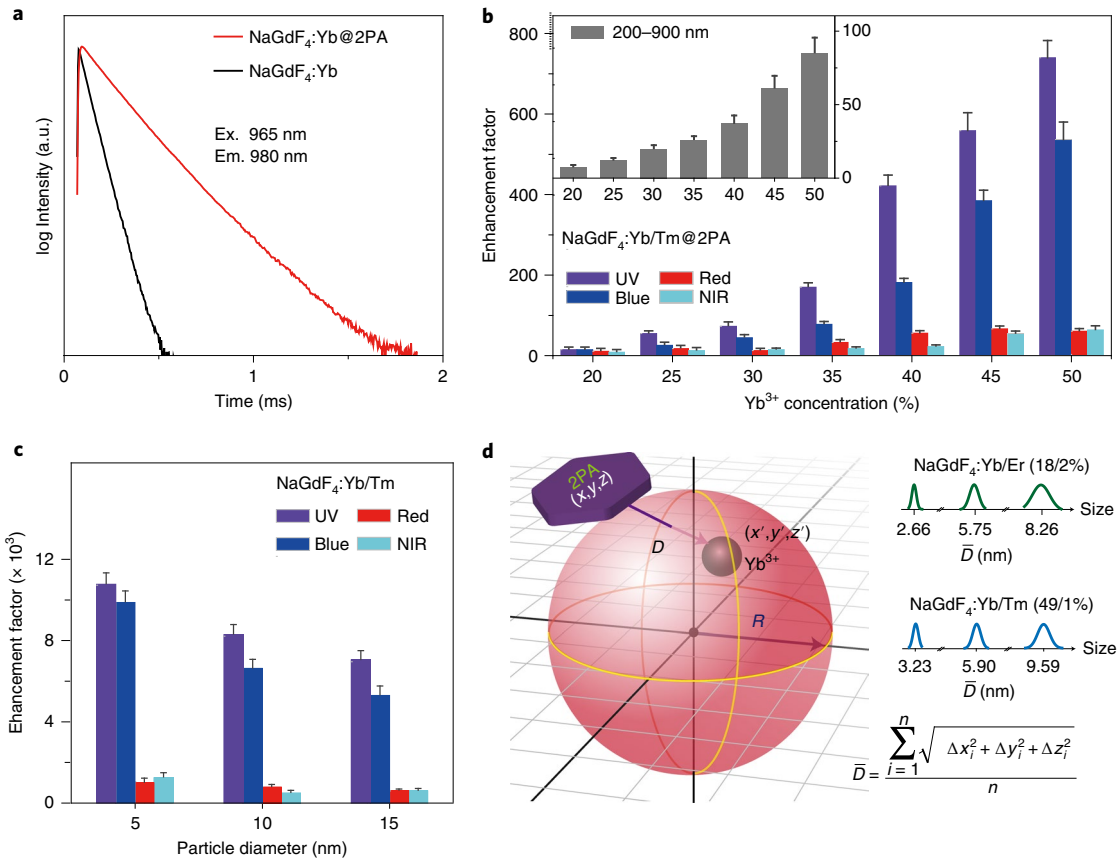

Fig. 2 | Optical investigations of upconversion nanocrystals on surface coordination. a, Lifetime decay curves of 980 nm Yb^{3+} emission from ligand-free and 2PA-capped $NaGdF_4$:Yb (5%) nanoparticles (10 nm) excited at 965 nm. **b**, Luminescence enhancement factors at different emission wavelengths from 2PA-capped $NaGdF_4$:Yb/Tm (15 nm, 1% Tm^{3+}) with different Yb^{3+} concentrations. The inset shows the enhancement of the integrated upconversion emission from 200 to 900 nm. UV, ultraviolet; NIR, near-infrared. Error bars represent the standard deviation of the luminescence enhancement factor. **c**, Calculated luminescence enhancement factors of the 2PA-capped $NaGdF_4$:Yb/Tm (49/1%) nanoparticles. Error bars represent the standard deviation of the luminescence enhancement factor. **d**, Average distances ($\bar{D}$) between the ligands and randomly doped lanthanide ions in nanoparticles with diameters of 5, 10 and 15 nm.

To better understand ligand-coordination effects, we prepared 2PA-capped $NaGdF_4$:Yb/Tm nanoparticles with different Yb^{3+} concentrations. Comparative photoluminescence results revealed that it is possible to achieve large enhancement factors in upconversion nanoparticles with high Yb^{3+} concentrations (Fig. 2b). The overall emission enhancement was dominated by enhanced emissions at 360 (UV) and 475 nm (blue), indicative of a strengthened multiphoton upconversion process. By contrast, the emission enhancement was relatively insensitive to Tm^{3+} concentration (Supplementary Fig. 16). A similar multiphoton upconversion enhancement was observed from the Er^{3+} emitter (Supplementary Fig. 17). Together, these results indicate that a high Yb^{3+} concentration promotes energy transfer from the sensitizers to the activators on ligand coordination to nanoparticles.

To evaluate the size-dependent luminescence enhancement quantitatively, we further prepared 2PA-capped $NaGdF_4$ nanoparticles of different sizes (5, 10, and 15 nm). Our results corroborated the increasing ligand-coordination effect in smaller nanocrystals (Fig. 2c and Supplementary Fig. 18). Importantly, the overall enhancement was dominated by increased emission in the UV and blue spectral regions, consistent with the dominant effect of ligand coordination on multiphoton upconversion (Fig. 2c). The UV emission was enhanced by 11,000-fold in the 5 nm $NaGdF_4$:Yb/Tm nanoparticles. As the ligand densities were similar on different-sized nanoparticles, the size-dependent enhancement was mainly attributed to the short mean distance between the Yb^{3+} ions and ligands in the small nanoparticles, which was corroborated by Monte Carlo simulation (Fig. 2d, Supplementary Figs. 19–22 and Supplementary Tables 4 and 5).

To further understand the ligand-coordination effect on upconversion processes, we measured the emission intensities of $NaLnF_4$:Yb/Er (Ln = Y or Gd) nanoparticles capped with a wide variety of ligands (Fig. 3a). The 2PA ligand yielded the largest enhancement factor (Fig. 3b). The enhancement factor of all ligands increased with decreasing particle size, and the ligand-coordination effect dominated in gadolinium-based host lattices. When nanoparticles were coated with flexible ligands such as heptanoic acid (HA), the increase in emission intensity was small (Fig. 3b). By contrast, nanoparticles capped with less flexible ligands (cyclohexanecarboxylic acid (CHA) or 2-phenylacetic acid (PAA)) achieved higher enhancement factors, suggesting that rigid ligands can obstruct interactions between nanoparticles and solvent molecules more effectively than flexible ligands. Moreover, numerous C–H bonds in the HA ligand facilitate non-radiative recombination via vibronic coupling to high-energy phonons[35]. Such non-radiative recombination partially counteracts the passivation-induced emission enhancement.

We next examined the enhancement factors for a series of nanoparticles capped with thiophenyl-, phenyl-, naphthyl- and methoxy-functionalized ligands (thiophene-2-carboxylic acid

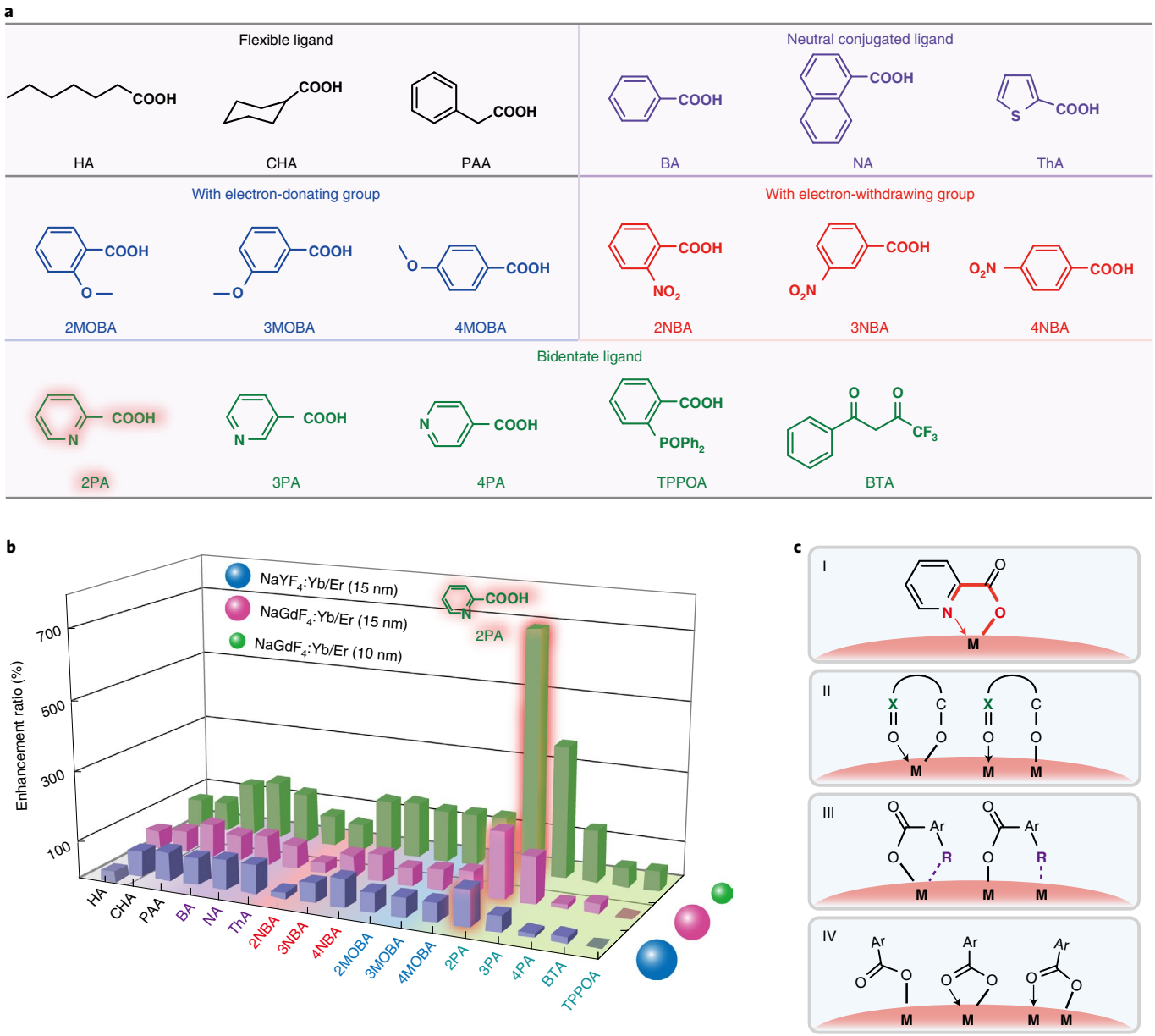

Fig. 3 | Ligand-coordination effects on upconversion luminescence enhancement. a, Structures of the ligands coordinating to the nanoparticles. **b**, Luminescence enhancement factors of three types of nanoparticles capped with various ligands. Nanoparticles were dissolved in ethanol and excited at 980 nm. Each experiment was repeated five times and the intensities were averaged to calculate the enhancement factors. **c**, Schematics of various metal–ligand coordination modes: (I) chelate mode with a five-membered ring (M = metal ion); (II) unsymmetrical bidentate mode (X = C or P atom); (III) substitution-assisted mode with inductive effects (R = substitutional group); and (IV) three coordination modes involving carboxylic acid ligands.

(ThA), benzoic acid (BA), 1-naphthoic acid (NA) and methoxybenzoic acid (MOBA) isomers). These ligands represent a sequential increase in molecular volume. When the ligand coordination reached saturation, all ligands exhibited similar enhancement factors. Moreover, variations in the substitution position of the electron-donating methoxy group of the MOBA ligand did not change the enhancement factor.

When the methoxy group was replaced with an electron-withdrawing nitro group, the *ortho*-substitution yielded a higher emission intensity than the *meta*- and *para*-substitutions. The enhancement factor increased from 0.5 in 2-nitrobenzoic acid (2NB) to 1.8 in 4-nitrobenzoic acid (4NBA), comparable to that observed in BA-capped nanoparticles. Substitution with highly polarized groups is likely to distort the surface sublattices and affect the coordination geometry of the surface Yb^{3+} ions, partially counteracting passivation-induced enhancement. By contrast, weakly polarized, rigid ligands enhanced the emission intensity by approximately twofold, similar to the enhancement achieved by surface passivation using silica or the polyvinylpyrrolidone polymer.

We further coated the nanoparticles with ligands that support different chelation modes (Fig. 3c). After bidentate chelation with 2PA molecules, the emission enhancement was fivefold higher than after monodentate chelation with carboxyl-containing molecules. We then optically characterized the nanoparticles coated with BA molecules, which have a similar molecular rigidity to the 2PA ligands but a different coordination mode. The lifetime of the 980 nm emission was slightly prolonged after coating with BA molecules, suggesting that monodentate chelation with BA is less

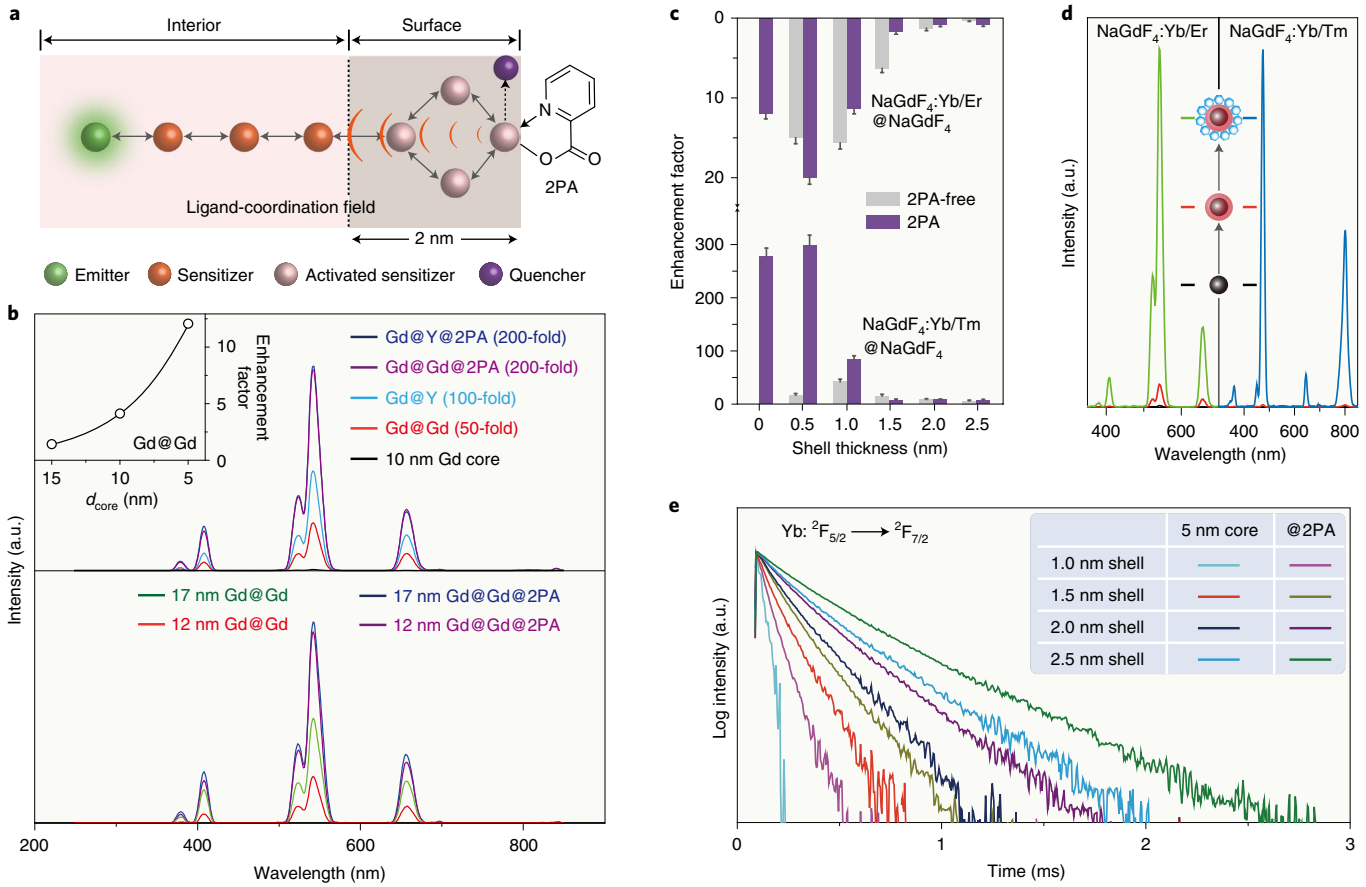

Fig. 4 | Long-range effect of ligand coordination on upconversion luminescence. a, Schematic showing the prolonged energy diffusion within sensitizer sublattices on ligand coordination. Solid grey and dotted black arrows denote enhanced energy transfer and suppressed non-radiative decay, respectively. **b**, Photoluminescence spectra of ligand-free and 2PA-capped $NaGdF_4$:Yb/Er(18/2%)@$NaLnF_4$ (Ln = Y or Gd) nanoparticles of different diameters. The shell thickness is approximately 1 nm. The numbers in parentheses are the enhancement factors relative to the bare-core emissions. The inset shows the core-size-dependent emission enhancement in $NaGdF_4$:Yb/Er@$NaGdF_4$ nanoparticles. d_{core}, core diameter. **c**, Emission enhancement factors of core–shell $NaGdF_4$ nanoparticles with different shell thicknesses, prepared via layer-by-layer growth on a 5 nm core. The layer thickness is 0.5 nm. Error bars denote the standard deviation of the luminescence enhancement factor. **d**, Photoluminescence spectra of ligand-free nanoparticles (5 nm core; black spectra), core–shell nanoparticles (0.5 nm shell; red spectra) and 2PA-capped core–shell nanoparticles (green and blue spectra). **e**, Time-resolved decay curves of 980 nm emission from Yb^{3+} ions doped in a series of $NaGdF_4$:Yb/Er(18/2%)@$NaGdF_4$ nanoparticles with different shell thicknesses, measured before and after 2PA surface coordination under 970 nm irradiation.

effective in stabilizing the excited state of Yb^{3+} ions than bidentate chelation with 2PA (Supplementary Figs. 4 and 12). DFT calculations indicate that the ytterbium 4*f* orbitals weakly hybridize with the BA molecular orbitals. Emissions can be influenced not only by the chelation mode but also by the polarity of the chelation site. For instance, the use of 4,4,4-trifluoro-1-phenylbutane-1,3-dione (BTA) and 2-(diphenylphosphoryl)benzoic acid (TPPOA) molecules comprising high-polarity sites, such as β-diketone and phosphine oxide, did not alter the nanoparticle emission, despite the unsymmetrical mode of O,O-bidentate chelation. Together, these results suggest that ligands with high rigidity, limited polarity and multidentate coordination can substantially enhance the upconversion intensity.

To determine the effective distance of the ligand-coordination field propagating through the surface layers, we synthesized core–shell nanoparticles with inert shells of various thicknesses separating the ligands from the outermost Yb^{3+} ions (Fig. 4a and Supplementary Figs. 23–25). As measured from the emission intensities and their corresponding enhancement factors in the 2PA-capped $NaGdF_4$@$NaGdF_4$ model system, the ligand coordination influenced the lanthanide sensitization even with a 2 nm shell (Fig. 4b,c). In the system with a 0.5 nm shell, luminescence was enhanced 3,000-fold (Fig. 4d and Supplementary Fig. 26).

We characterized the as-prepared hybrid nanoparticles using time-resolved spectroscopy. The measured 980 nm decay profile of the Yb^{3+} ions indicated that both the ligand and the shell prolonged the lifetime of the sensitizer's excited states (Fig. 4e). The decay curve of the Er^{3+} emission was similarly prolonged by the ligand and the shell (Supplementary Fig. 27). Moreover, the Er^{3+} emission of the as-prepared nanoparticles exhibited a slow rise, suggesting a long-lived intermediate state that prolongs energy pumping to the Er^{3+} emitters. A similar decay trend was observed in the Tm^{3+}/Yb^{3+}-codoped nanoparticles (Supplementary Fig. 28). By comparison, the lifetime of the Tm^{3+} emission was more sensitive to surface coordination than that of the Er^{3+} emission, consistent with the observed emission intensity enhancement (Fig. 4c). These results imply that the blue emission is more dominated by 2PA-mediated surface coordination than shell-induced passivation.

In conclusion, we have presented a general ligand-coordination strategy that enhances multiphoton upconversion in ultrasmall nanocrystals by reconstructing orbital hybridization and

crystal-field splitting in surface lanthanides. Ligand coordination can activate the sensitizer-containing surface layer, improving the efficiency of energy-transfer-mediated upconversion. The effect is dominant in ultrasmall nanoparticles doped with high concentrations of sensitizers. By combining the long-range coordination effect with thin-shell passivation, the overall emission can be greatly enhanced. For instance, the overall emission intensity was 3,000 times higher in 2PA-coated $NaGdF_4$:Yb/Tm@$NaGdF_4$ nanocrystals than in the 5 nm bare core. Unlike conventional core–shell engineering and dye-sensitization methods, the ligand-coordination strategy neither affects the nanocrystal size nor requires spectral overlap between the lanthanide absorption and the dye emission. The fundamentals gained from our investigations may provide insight into utilizing 4*f* electrons for chemical bonding and benefit the design of high-performance organic–inorganic hybrid luminescent nanomaterials.

Online content

Any methods, additional references, Nature Research reporting summaries, source data, extended data, supplementary information, acknowledgements, peer review information; details of author contributions and competing interests; and statements of data and code availability are available at https://doi.org/10.1038/s41566-021-00862-3.

Received: 23 January 2021; Accepted: 17 July 2021;
Published online: 9 September 2021

References

1. Auzel, F. Upconversion and anti-Stokes processes with *f* and *d* ions in solids. *Chem. Rev.* **104**, 139–174 (2004).
2. Zhou, J., Liu, Q., Feng, W., Sun, Y. & Li, F. Upconversion luminescent materials: advances and applications. *Chem. Rev.* **115**, 395–465 (2015).
3. Gargas, D. J. et al. Engineering bright sub-10-nm upconverting nanocrystals for single-molecule imaging. *Nat. Nanotechnol.* **9**, 300–305 (2014).
4. Rabouw, F. T. et al. Quenching pathways in $NaYF_4$:Er^{3+},Yb^{3+} upconversion nanocrystals. *ACS Nano* **12**, 4812–4823 (2018).
5. Mei, S. et al. Networking state of ytterbium ions probing the origin of luminescence quenching and activation in nanocrystals. *Adv. Sci.* **8**, 2003325 (2021).
6. Bünzli, J.-C. G. & Piguet, C. Taking advantage of luminescent lanthanide ions. *Chem. Soc. Rev.* **34**, 1048–1077 (2005).
7. Dong, H., Sun, L. D. & Yan, C. H. Energy transfer in lanthanide upconversion studies for extended optical applications. *Chem. Soc. Rev.* **44**, 1608–1634 (2015).
8. Carneiro Neto, A. N., Moura, R. T. & Malta, O. L. On the mechanisms of nonradiative energy transfer between lanthanide ions: centrosymmetric systems. *J. Lumin.* **210**, 342–347 (2019).
9. Shyichuk, A. et al. Energy transfer upconversion dynamics in YVO_4:Yb^{3+},Er^{3+}. *J. Lumin.* **170**, 560–570 (2016).
10. Wu, S. et al. Non-blinking and photostable upconverted luminescence from single lanthanide-doped nanocrystals. *Proc. Natl Acad. Sci. USA* **106**, 10917–10921 (2009).
11. Liu, Q. et al. Single upconversion nanoparticle imaging at sub-10 W cm^{-2} irradiance. *Nat. Photonics* **12**, 548–553 (2018).
12. Lee, J. et al. Universal process-inert encoding architecture for polymer microparticles. *Nat. Mater.* **13**, 524–529 (2014).
13. Bettinelli, M., Carlos, L. & Liu, X. Lanthanide-doped upconversion nanoparticles. *Phys. Today* **68**, 38–44 (2015).
14. Chen, X. et al. Confining energy migration in upconversion nanoparticles towards deep ultraviolet lasing. *Nat. Commun.* **7**, 10304 (2016).
15. Liu, Y. et al. Amplified stimulated emission in upconversion nanoparticles for super-resolution nanoscopy. *Nature* **543**, 229–233 (2017).
16. Dong, H. et al. Lanthanide nanoparticles: from design toward bioimaging and therapy. *Chem. Rev.* **115**, 10725–10815 (2015).
17. Fan, Y. et al. Lifetime-engineered NIR-II nanoparticles unlock multiplexed in vivo imaging. *Nat. Nanotechnol.* **13**, 941–946 (2018).
18. Chen, S. et al. Near-infrared deep brain stimulation via upconversion nanoparticle-mediated optogenetics. *Science* **359**, 679–684 (2018).
19. Chu, H., Zhao, J., Mi, Y., Di, Z. & Li, L. NIR-light-mediated spatially selective triggering of anti-tumor immunity via upconversion nanoparticle-based immunodevices. *Nat. Commun.* **10**, 2839 (2019).
20. Quintanilla, M., Ren, F., Ma, D. & Vetrone, F. Light management in upconverting nanoparticles: ultrasmall core/shell architectures to tune the emission color. *ACS Photonics* **1**, 662–669 (2014).
21. Zhang, Y. et al. Ultrasmall-superbright neodymium-upconversion nanoparticles via energy migration manipulation and lattice modification: 808 nm-activated drug release. *ACS Nano* **11**, 2846–2857 (2017).
22. Bian, W. et al. Direct identification of surface defects and their influence on the optical characteristics of upconversion nanoparticles. *ACS Nano* **12**, 3623–3628 (2018).
23. Ma, C. et al. Optimal sensitizer concentration in single upconversion nanocrystals. *Nano Lett.* **17**, 2858–2864 (2017).
24. Wu, D. M., García-Etxarri, A., Salleo, A. & Dionne, J. A. Plasmon-enhanced upconversion. *J. Phys. Chem. Lett.* **5**, 4020–4031 (2014).
25. Fernandez-Bravo, A. et al. Ultralow-threshold, continuous-wave upconverting lasing from subwavelength plasmons. *Nat. Mater.* **18**, 1172–1176 (2019).
26. Zhao, J. et al. Single-nanocrystal sensitivity achieved by enhanced upconversion luminescence. *Nat. Nanotechnol.* **8**, 729–734 (2013).
27. Liang, L. et al. Upconversion amplification through dielectric superlensing modulation. *Nat. Commun.* **10**, 1391 (2019).
28. Strange, P., Svane, A., Temmerman, W. M., Szotec, Z. & Winter, H. Understanding the valency of rare earths from first-principles theory. *Nature* **399**, 756–758 (1999).
29. Zhou, J. et al. Activation of the surface dark-layer to enhance upconversion in a thermal field. *Nat. Photonics* **12**, 154–158 (2018).
30. Blasse, G. Energy migration in rare-earth compounds. *Recl. Trav. Chim. Pays Bas* **105**, 143–149 (1986).
31. Zuo, J. et al. Precisely tailoring upconversion dynamics via energy migration in core–shell nanostructures. *Angew. Chem. Int. Ed.* **57**, 3054–3058 (2018).
32. Chen, X. et al. Energy migration upconversion in Ce(III)-doped heterogeneous core–shell–shell nanoparticles. *Small* **13**, 1701479 (2017).
33. Garfield, D. J. et al. Enrichment of molecular antenna triplets amplifies upconverting nanoparticle emission. *Nat. Photonics* **12**, 402–407 (2018).
34. Han, S. et al. Lanthanide-doped inorganic nanoparticles turn molecular triplet excitons bright. *Nature* **587**, 594–599 (2020).
35. Bünzli, J. C. G. On the design of highly luminescent lanthanide complexes. *Coord. Chem. Rev.* **293–294**, 19–47 (2015).

Methods

Nanoparticle synthesis. Lanthanide-doped nanoparticles were synthesized as described in a previous report[36]. Additional experimental details are provided in the Supplementary Information.

Transmission electron microscopy characterization. Transmission electron microscopy measurements were performed using a field-emission transmission electron microscope (JEOL-JEM 2010F) operated at an acceleration voltage of 200 kV.

Absorption and luminescence spectroscopy analysis. Absorption spectra in the near-infrared range were measured at room temperature using a UV–visible–NIR spectrophotometer (UV3600, Shimadzu). Photoluminescence spectra were recorded at room temperature using a DM150i monochromator equipped with an R928 photon-counting photomultiplier tube, in conjunction with a 980 nm diode laser. Decay curves were measured using a customized UV-to-mid-infrared phosphorescence lifetime spectrometer (FSP920-C, Edinburgh Instruments) equipped with a digital oscilloscope (TDS3052B, Tektronix) and a tunable mid-band optical parametric oscillator laser as the excitation source (410–2,400 nm; Vibrant 355II, OPOTEK).

First-principles calculations. Quantum mechanical calculations were conducted on the basis of the mathematical framework of DFT using the Vienna ab initio package with the projector augmented wave method[37]. Throughout the calculations, the Perdew–Burke–Ernzerhof generalized gradient approximation was employed and a 12% Hartree–Fock exchange interaction was included through the use of the screened-exchange hybrid density functional HSE06. Additional calculation details are provided in the Supplementary Information.

Data availability

All relevant data that support the findings of this work are available from the corresponding author on reasonable request.

Code availability

First-principles calculations were performed using the commercially available Vienna Ab initio Simulation Package. The codes used to calculate the distance between lanthanide ions and ligands are provided in the Supplementary Information.

References

36. Johnson, N. J. J., Korinek, A., Dong, C. & van Veggel, F. C. J. M. Self-focusing by Ostwald ripening: a strategy for layer-by-layer epitaxial growth on upconverting nanocrystals. *J. Am. Chem. Soc.* **134**, 11068–11071 (2012).
37. Kresse, G. & Furthmüller, J. Efficiency of ab-initio total energy calculations for metals and semiconductors using a plane-wave basis set. *Comput. Mater. Sci.* **6**, 15–50 (1996).

Acknowledgements

X.L. acknowledges support from the NUS NANONASH Programme (NUHSRO/2020/002/NanoNash/LOA; R143000B43114), the Singapore Ministry of Education (MOE2017-T2-2-110) and the Agency for Science, Technology and Research (A*STAR) (grant no. A1883c0011). H.X. acknowledges support from the National Natural Science Foundation of China (NSFC) (grant no. 92061205) and Young Innovative Team Supporting Projects of Heilongjiang Province.

Author contributions

H.X., X.Q. and X.L. conceived, designed and supervised the project and led the collaboration efforts. H.X. and S.H. synthesized the nanocrystals and conducted the optical experiments with contributions from R.D., Q.S. and Y.T. Quantum mechanical calculations were conducted by X.Q. Monte Carlo simulations were performed by Y.W. The manuscript was written by H.X., X.Q., S.H. and X.L. All authors participated in the discussion and analysis of the manuscript.

Competing interests

The authors declare no competing interests.

Additional information

Supplementary information The online version contains supplementary material available at https://doi.org/10.1038/s41566-021-00862-3.

Correspondence and requests for materials should be addressed to Hui Xu, Xian Qin or Xiaogang Liu.

Peer review information *Nature Photonics* thanks Marco Bettinelli, Dayong Jin and the other, anonymous, reviewer(s) for their contribution to the peer review of this work.